Mon. Not. R. Astron. Soc. **000**, 1–15 (2002) Printed 25 May 2004 (MN LATEX style file v2.2)

Mapping stationary axisymmetric phase-space distribution functions by orbit libraries

J. Thomas[1⋆], R. P. Saglia[1,2], R. Bender[1,2], D. Thomas[2], K. Gebhardt[3], J. Magorrian[4], D. Richstone[5]
[1] *Universitätssternwarte München, Scheinerstraße 1, D-81679 München, Germany*
[2] *Max-Planck-Institut für Extraterrestrische Physik, Giessenbachstraße, D-85748 Garching, Germany*
[3] *Department of Astronomy, University of Texas at Austin, C1400, Austin, TX78712, USA*
[4] *Theoretical Physics, Department of Physics, University of Oxford, 1 Keble Road, Oxford U.K., OX1 3NP*
[5] *Department of Astronomy, Dennison Bldg., University of Michigan, Ann Arbor 48109*

Accepted 1988 December 15. Received 1988 December 14; in original form 1988 October 11

ABSTRACT
This is the first of a series of papers dedicated to unveil the mass composition and dynamical structure of a sample of flattened early type galaxies in the Coma cluster. We describe our modifications to the Schwarzschild code of Richstone et al. (in preparation). Applying a Voronoi tessellation in the surface of section we are able to assign accurate phase-space volumes to individual orbits and to reconstruct the full three-integral phase-space distribution function (DF) of any axisymmetric orbit library. Two types of tests have been performed to check the accuracy with which DFs can be represented by appropriate orbit libraries. First, by mapping DFs of spherical γ-models and flattened Plummer models on to the library we show that the resulting line-of-sight velocity distributions and internal velocity moments of the library match those directly derived from the DF to a precision better than that of present day observational errors. Second, by fitting libraries to the projected kinematics of the same DFs we show that the distribution function reconstructed from the fitted library matches the input DF to a rms of about 15 per cent over a region in phase-space covering 90 per cent of the mass of the library. The achieved accuracy allows us to implement effective entropy-based regularisation to fit real, noisy and spatially incomplete data.

Key words: stellar dynamics – galaxies: elliptical and lenticular, cD – galaxies: kinematics and dynamics — galaxies: structure

1 INTRODUCTION

Since the pioneering work of Schwarzschild (1979) orbit superposition techniques have become an important tool in the dynamical modelling of spheroidal stellar systems. Stationary distribution functions (DFs) of such systems are subject to Jeans' theorem and hence depend on the phase-space coordinates only via the integrals of motion. In the axisymmetric case these integrals are energy E, angular momentum along the axis of symmetry L_z and for most potentials an additional, non-classical "third integral" I_3. Because any set of integrals of motion essentially represents an orbit and vice versa, the DF can be approximated by the sum of single-orbit DFs, with the only adjustable parameter being the total amount of light carried by the orbit. The main task that remains to adequately describe hot stellar systems is to find an appropriate set of orbits.

Orbit superposition techniques have been used to model such systems in various symmetries (e.g. Rix et al. 1997; Romanowsky & Kochanek 1997; van der Marel et al. 1998; Cretton et al. 1999; Cappellari et al. 2002; Verolme et al. 2002; Gebhardt et al. 2003; van de Ven et al. 2003), with the goal of determining different dynamical parameters like central black hole masses, internal velocity anisotropy or global mass-to-light ratios. An orbit library tracing the phase-space structure of a trial potential is fitted to observed photometry and kinematics, to decide, whether or not it gives a valid model of the corresponding galaxy.

In the spherical case there exists a well-known mass-anisotropy degeneracy permitting in general convincing fits to the projected velocity dispersion σ even if the trial potential differs from the true one (Binney & Mamon 1982). With complete knowledge of the full line-of-sight velocity distri-

⋆ E-mail:jthomas@mpe.mpg.de

butions (LOSVDs) however, it is possible to reconstruct the DF, given the potential is known (Dejonghe & Merritt 1992). Furthermore, even for the realistic case where the potential is not known in advance Merritt & Saha (1993) and Gerhard (1993) have shown how the information contained in the LOSVDs can constrain both, the potential and the DF.

Likewise, in the axisymmetric case, Dehnen & Gerhard (1993) have calculated realistic smooth DFs and have shown that a similarily close relationship exists between the potential and internal kinematics on the one side and the projected kinematics on the other side. However, fits of axisymmetric libraries still pose some additional open questions. Recently, Valluri, Merritt & Emsellem (2004) discussed the indeterminacy of the reconstruction of the potential in general axisymmetric systems from two- or three-dimensional data sets, by studying the shape of the χ^2-contours describing the quality of the orbital fit. Cretton & Emsellem (2004) argued that even in case of a mathematically non-degenerate $f(E, L_z)$-system an artificial degeneracy occurs, caused by the discreteness of the orbit library and emphasized the role of appropriate smoothing, although not providing a definite solution. Richstone et al. (2004) critically analysed their arguments and emphasized that both high quality comprehensive data sets and orbit libraries are needed to achieve a reliable modeling of axisymmetric systems.

In view of this discussion concerning orbit-based dynamical models it seems worthwhile to step back and investigate how well orbit libraries represent the phase-space structure of a given dynamical system. This includes the examination of the choice of orbits, which in the generic axisymmetric case is difficult, since part of the phase-space structure is unknown due to our ignorance related to I_3. A key tool for such an analysis are the orbital phase-volumes which accomplish the transformation from the relative contributions of individual orbits to the library, the so called orbital occupation numbers or orbital weights, into phase-space densities (and vice versa). The availability of such phase-volumes actually offers several applications:

(i) Accurate phase-volumes allow to calculate internal and projected properties like density and velocity profiles, line-of-sight velocity distributions (LOSVDs) etc. of general axisymmetric DFs $f(E, L_z, I_3)$ via orbit libraries. Besides the possibility to systematically study the structure of general axisymmetric systems, these profiles provide a direct check of the choice of orbits via their comparison with those calculated from directly integrating the DFs.

(ii) From any fitted library one can reconstruct the corresponding DF via the phase-volumes and thus reconstruct the DF from any observed early-type galaxy in the axisymmetric approximation.

(iii) If the library is fitted to some reference data constructed from a DF, then (ii) allows to investigate how closely the fit matches the input DF and to implement an effective regularisation scheme, permitting to fit real (noisy) data sets.

Vandervoort (1984) touched the problem by writing down the transformation from cells of integrals to the corresponding phase-space volumes. However, the resulting relations are only suitable for explicitly known integrals, e.g. for single orbits only in the rare case all integrals are known. For components integrated about the unknown integrals they have been exploited by e.g. Rix et al. (1997), Cretton et al. (1999) and Verolme & de Zeeuw (2002).

The aim of the present paper is to introduce a general implementation for the calculation of individual orbital phase-volumes in any axisymmetric potential and, by following applications (i) and (iii) to prove that our libraries accurately map given dynamical systems. This directly justifies our setup of the library and sets the basis for our project to recover the dynamical structure and mass composition of a sample of flattened early-type galaxies in the Coma cluster. In a subsequent paper we will focus on the question of how much smoothing has to be applied in order to get an optimal estimate of the dynamical system underlying a given set of noisy and spatially incomplete observational data. The full analysis of the data set (Mehlert et al. 2000; Wegner et al. 2002) will be addressed in a future publication.

The paper is organized as follows. In Sec. 2 we define all quantities related to the library used in the subsequent Sections and describe our orbit sampling. Sec. 3 outlines the relation between orbital weights and orbital phase-space densities. Sec. 4 contains a description of our implementation to calculate individual orbital phase-space volumes. In a first application we calculate internal and projected properties of given DFs using orbit libraries in Sec. 5. Sec. 6 discusses how the library is fitted to given data sets and in Sec. 7 we reconstruct reference DFs from their projected kinematics. Finally, Sec. 8 summarizes the results.

2 THE ORBIT LIBRARY

Our method to set up the orbit libraries used for the dynamical modelling is based on the procedure presented in Richstone et al. (in preparation). There, the reader finds a description of the basic properties of the program. In this section we define quantities that are used later on in this paper.

In the following we assume that the luminosity density ν is known. In the analysis of real data it has to be obtained by deprojection of the measured photometry. With the stellar mass-to-light ratio $\Gamma = (\frac{M}{L})$ the mass density ρ_l of the luminous material follows from ν as $\rho_l = \Gamma\,\nu$.

The total mass density ρ possibly includes a dark component $\rho_{\rm DM}$ and reads

$$\rho = \rho\,(\Gamma, r_c, v_c) = \Gamma\,\nu + \rho_{\rm DM} \tag{1}$$

Once the mass-profile is fixed, the potential Φ follows by integrating Poisson's equation. With Φ known, a large set of orbits is calculated, sampling homogeneously the phase-space connected with Φ.

2.1 Spatial and velocity binning

As described in Richstone et al. (in preparation) we divide the meridional plane into bins, equally spaced in $\sin\vartheta$[1], linear in r near the inner boundary $r_{\rm min}$ of the library and

[1] Throughout the paper, we use spherical coordinates (r, ϑ, φ), with $\vartheta = 0^\circ$ corresponding to the equatorial plane. If not stated otherwise, we use super- or subscripts h, i, j, k as indices, l, m, n as exponents.

logarithmic at the outer boundary $r_{\max}$, (if not stated otherwise we use $N_r = 20$ radial bins, $N_\vartheta = 5$ angular bins.) For the projection of the library we use the same binning as for the meridional plane. Every spatial bin in the plane of the sky is subdivided into $N_{\rm vel}$ bins linearly spaced in projected velocities between $-v_{\max}$ and $v_{\max}$, leading to a binsize for the LOSVDs of

$$\Delta v_{\rm LOSVD} = 2\frac{v_{\max}}{N_{\rm vel}}. \tag{2}$$

Even if the potential is spherical, then our spatial binning tags an axis of symmetry. Later, when referring to a "minor-axis" we always mean the axis $\vartheta = 90°$ of the library.

2.2 Orbital properties

Luminosity. For every orbit i in the library we store its normalized contribution to the luminosity dL_i^j in spatial bin $1 \leqslant j \leqslant N_r \times N_\vartheta$, which equals the fraction of time the orbit spends in bin j. Let Δt_i^k denote the k-th timestep in the integration of orbit i, so that

$$t_i^k \equiv \sum_{h \leqslant k} \Delta t_i^h \tag{3}$$

is the total time elapsed until timestep k and

$$\mathcal{J}^j \equiv \{k : (r(t_i^k), \vartheta(t_i^k)) \in \mathrm{bin}\, j\} \tag{4}$$

contains all timesteps during which orbit i is located in spatial bin j. Accordingly, we can write

$$\mathrm{dL}_i^j = \sum_{k \in \mathcal{J}^j} \frac{\Delta t_i^k}{T_i}, \tag{5}$$

with $T_i \equiv \sum \Delta t_i^k$ being the total integration time of orbit i.

Given the orbit's weight w_i to the whole library – the integrated luminosity along the orbit – the total luminosity of the library in spatial bin j reads

$$\mathrm{dL}^j = \sum_i w_i \, \mathrm{dL}_i^j. \tag{6}$$

Internal velocity moments. To obtain the internal velocity moments $\left\langle v_r^l v_\vartheta^m v_\varphi^n \right\rangle$ of the orbit library, we store for each orbit i and each time step Δt_i^k the product of velocities $v_r^l v_\vartheta^m v_\varphi^n$ and fractional time $\Delta t_i^k / T_i$. All contributions in spatial bin j are summed up to yield

$$\left\langle v_r^l v_\vartheta^m v_\varphi^n \right\rangle_i^j \equiv \sum_{k \in \mathcal{J}^j} v_r^l v_\vartheta^m v_\varphi^n \, \frac{\Delta t_i^k}{T_i}. \tag{7}$$

Thus for the whole library the velocity moments in spatial bin j follow as

$$\left\langle v_r^l v_\vartheta^m v_\varphi^n \right\rangle^j = \frac{1}{\mathrm{d}L^j} \sum_i w_i \left\langle v_r^l v_\vartheta^m v_\varphi^n \right\rangle_i^j. \tag{8}$$

Projected kinematics. For the projected kinematics of the library we record the normalized contribution to the kinematics LOSVD_i^{jk} at projected position j and projected velocity $1 \leqslant k \leqslant N_{\rm vel}$ for every orbit. Again for the whole library the LOSVD reads

$$\mathrm{LOSVD}^{jk} = \sum_i w_i \, \mathrm{LOSVD}_i^{jk}. \tag{9}$$

By fitting a Gauss-Hermite series to the LOSVD^{jk} we obtain the Gauss-Hermite parameters (Gerhard 1993; van der Marel & Franx 1993)

$$\mathrm{GHP}^{jk} = \{\gamma^{jk}, v^{jk}, \sigma^{jk}, H_3^{jk}, H_4^{jk}\} \tag{10}$$

of the LOSVD.

2.3 Choice of orbits

To obtain a reliable representation of phase-space it is important that any allowed combination of the integrals of motion (E, L_z, I_3) is represented to some degree of approximation by an orbit in the library. The absence of some orbit family in the library might misleadingly emphasize certain dynamical configurations in the final fit.

Sampling E and L_z. Richstone et al. (in preparation) adjust the orbit sampling in (E, L_z)-space according to their spatial binning. From the requirement that every pair of grid bins $r_i \leqslant r_j$ in the equatorial plane should be connected by at least one equatorial orbit with $r_{\rm peri} = r_i$ and $r_{\rm apo} = r_j$ they uniquely derive a grid of orbital energies E and z-angular momenta L_z. We experimented with doubling the number of peri- and/or apocenters per radial bin but found that the above described method yields a sufficiently dense sampling of the (E, L_z)-plane.

Sampling I_3. It is common practice among the various existing Schwarzschild codes to sample I_3 by dropping orbits at given energy E and angular momentum L_z from the zero-velocity-curve (ZVC, defined by $E = L_z^2/(2r^2 \cos^2\vartheta) + \Phi(r, \vartheta)$). Richstone et al. (in preparation) use the intersections of the angular rays of the meridional grid with the ZVC as starting points. This sampling ensures that each sequence of orbits with common E and L_z contains at least one orbit that is roughly confined to the region between the equatorial plane and each angular ray of the meridional grid.

If we consider only potentials symmetrical about the equatorial plane with $\mathrm{d}\Phi/\mathrm{d}z > 0$, then every orbit eventually crosses the equatorial plane and leaves a footstep in the surface of section (SOS) given by the radii r and radial velocities v_r of the upward equatorial crossings. Orbits respecting a third integral show up in the SOS as nested invariant curves, sometimes with embedded resonances (e.g. Binney & Tremaine 1987). Fig. 1 shows an example of a SOS. The dots mark representative points of invariant curves obtained by numerically following orbits with common E and L_z in a flattened Hernquist potential with total mass $M = 10^{11}\,\mathrm{M}_\odot$, scaling radius $r_s = 10\,\mathrm{kpc}$ and a flattening of $q = 0.5$ (see Sect. 5.1 below for further details).

The SOS encompasses all available orbital shapes and a representative sampling of orbits should end up with the SOSs homogeneously filled with orbital imprints. Unfortunately, we are not aware of any simple relationship between the drop-point of an orbit on the ZVC and its corresponding appearance in the SOS, as long as I_3 is not known explicitly. In order to guarantee a representative collection of orbits in any case, we sample the orbits as follows.

In a first step we drop orbits from the (outer) intersections of the angular rays of our spatial grid with the ZVC as described in Richstone et al. (in preparation). Then, for any pair (E, L_z) included in the library we choose N_L radii r_l, $1 \leqslant l \leqslant N_L$ equally spaced in $\log(r)$ on the equatorial plane between $r_{\rm peri}$ and $r_{\rm apo}$ of the equatorial radial orbit with energy E and angular momentum L_z. We start with the smallest of these radii r_l and launch an orbit i from the equatorial plane with the maximal radial velocity

$$v_{r,i} = \sqrt{2\,(E - \Phi(r_l)) - \frac{L_z^2}{r_l^2}} \equiv v_{\max}(E, L_z, r_l). \qquad (11)$$

For the subsequent orbits i' we stepwise decrease $v_{r,i'}$ by $\Delta v_{r,i'}$ (see equation (13) below) until we reach $v_{r,i'} = 0$ and pass over to the next radius r_{l+1}.

With (E, L_z) and $(r_l, v_{r,i})$ fixed the orbital $v_{\vartheta,i}$ is determined by

$$v_{\vartheta,i}(E, L_z, r_l, v_{r,i}) = \sqrt{2\,(E - \Phi(r_l)) - v_{r,i}^2 - \frac{L_z^2}{r_l^2}}. \qquad (12)$$

When $v_{r,i} = 0$, then $v_{\vartheta,i}(E, L_z, r_l, v_{r,i}) = v_{\max}(E, L_z, r_l)$. For each velocity pair we launch an orbit from the equatorial plane at the actual r_l with the actual velocities $v_{r,i}$ and $v_{\vartheta,i}$. This procedure is repeated for each of the N_L radii. If, at a specific launch position, we find an imprint in the SOS of a previously integrated orbit which differs from the current launch position by less than 10 per cent in radius and radial velocity, then we regard this part of the SOS as already sampled and discard the orbit.

The velocity stepsize $\Delta v_{r,i}$ is set as

$$\Delta v_{r,i} = \min\left\{\Delta v_{\rm LOSVD}\,,\, \xi\; v_{m,i-1}\right\}, \qquad (13)$$

where $\Delta v_{\rm LOSVD}$ is the width of the LOSVD-bins (cf. equation (2)) and

$$v_{m,i} = \max_{1 \leqslant s \leqslant N_{\rm sos}} \{v_i^s : (r_i^s, v_i^s) \in {\rm SOS}\}. \qquad (14)$$

Here SOS denotes the set of the $N_{\rm sos}$ orbital imprints in the SOS and i is the index of the actual orbit. We usually take $\xi = 1/3.5$. Trying different values for N_L we found $N_L = 30$ sufficient to yield a dense filling of the SOS with approximately one invariant curve crossing the r-axis of the SOS in each of the equatorial meridional grid bins. The corresponding orbits have large ϑ-motion and need to be included in the library to avoid a radially biased collection of orbits.

The velocity stepsize is largest for the radial orbits and gradually decreases when the SOS is filled with orbits (note that $v_{m,i-1}$ is the maximum of the radial velocities in the SOS of the "precursor" orbit $i-1$). For the shell orbits, the stepsize becomes smallest. The adjustment of the stepsize in each step ensures that we sample the more radial orbits with a resolution that corresponds at least to the width of the LOSVD bins and that the sampling is refined for the shell orbits.

After the above described sampling is done, we measure the maximum f_s of all $r_{\min,i}/r_{\max,i}$, with

$$r_{\min,i} = \min_{1 \leqslant s \leqslant N_{\rm sos}} \{r_i^s : (r_i^s, v_i^s) \in {\rm SOS}\} \qquad (15)$$

and $r_{\max,i}$ defined analogously. To ensure that the sequence contains all orbits up to (approximately) the thin shell orbit, we complete the library if necessary by launching orbits from the equatorial plane with $v_r = 0$ at

$$r = \frac{3\,r_{\min,i'} + r_{\max,i'}}{4}, \qquad (16)$$

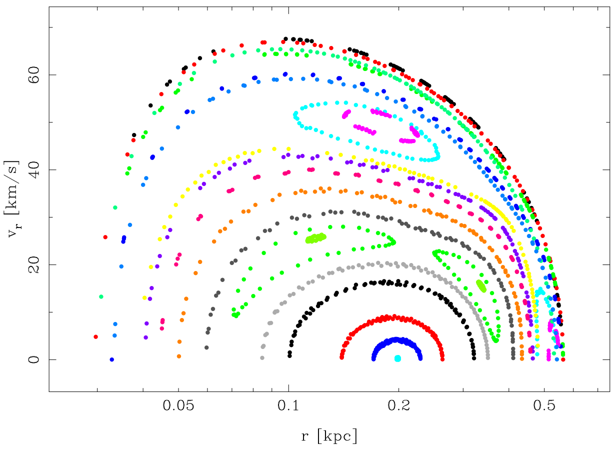

Figure 1. Example of a surface of section for a flattened Hernquist model (details in the text). All orbits have been integrated for $N_{\rm SOS} = 80$ intersections with the SOS.

where $f_s = r_{\min,i'}/r_{\max,i'}$, until $f_s > 0.9$.

Fig. 1 illustrates the dense coverage of the SOS with invariant curves after all orbits are integrated for a flattened Hernquist potential.

2.4 Use of the library

If the relative contribution of each orbit to the whole library, the orbital weight w_i, is specified, then according to equations (6), (8) and (9) the library provides a specific model including the LOSVDs, internal density distribution, internal velocity moments and so on of this particular orbit superposition.

If the library is constructed to test whether or not a given trial mass distribution leads to a consistent model of an observed galaxy, then the model, in particular the LOSVDs, have to be compared to the observations. If the comparison turns out not to yield a satisfactory fit, then the weights can either be recalculated (see Sec. 6 for details) or the actual mass distribution has to be rejected. If on the other hand, the fit shows that the actual set of weights seems to be a valid model of the galaxy, then one can reconstruct the internal velocity structure and DF from the w_i's.

Conversely, if one has a DF at hand and wants to calculate e.g. its projected kinematics without going through the appropriate integrals, one can assign the orbital weights according to the DF (see Sec. 5) without any fitting procedure and analyse the output of the library. This can be usefull to study systematically the projected properties of general axisymmetric distribution functions depending on all three integrals (E, L_z, I_3).

In the following we will make use of both applications with the goal to investigate the accuracy of our orbit libraries.

3 ORBITAL WEIGHTS AND PHASE-SPACE DENSITIES

In order to reconstruct the DF from the library or to calculate spatial profiles of internal or projected properties of some given DF, one needs to convert orbital weights into phase-space densities and vice versa. This section summarizes the connection between orbital weights and orbital phase-space densities under the regime of Jeans' theorem.

3.1 Phase-space densities of orbits

Consider a system in which the orbits respect n integrals of motion $I_1, \ldots, I_n$. Because the phase-space density of stationary systems is constant along individual orbits (Jeans theorem) the phase-space density along orbit i is given as the orbital weight w_i divided by the phase-space volume V_i. More formally, let $\mathcal{I}$ denote the n-dimensional set of orbital integrals $(I_1, \ldots, I_n)$, let $\mathcal{V}$ denote the 6-dimensional phase-space, $\mathcal{P}(\mathcal{V})$ its power set and let $\xi : \mathcal{I} \to \mathcal{P}(\mathcal{V})$ map a n-tuple of orbital integrals $(I_1, \ldots, I_n) \in \mathcal{I}$ on to the hypersurface $\xi(I_1, \ldots, I_n) \subseteq \mathcal{V}$ in phase-space covered by the corresponding orbit,

$$\xi(I_1, \ldots, I_n) \equiv \{p \in \mathcal{V} : I_1(p) = I_1, \ldots, I_n(p) = I_n\}. \tag{17}$$

With $\mathcal{U}_i \subseteq \mathcal{I}$ being the small cell in integral space represented by the orbit i,

$$\begin{aligned}\mathcal{U}_i \equiv \{&(I_1, \ldots, I_n) \in \mathcal{I} : I_1 \in [I_{1,i} - \Delta I_{1,i}, I_{1,i} + \Delta I_{1,i}], \\ &\ldots, I_n \in [I_{n,i} - \Delta I_{n,i}, I_{n,i} + \Delta I_{n,i}]\}\end{aligned} \tag{18}$$

we define the characteristic function

$$\chi_i \equiv \begin{cases} 1 & : \quad (r, \vartheta, \varphi, v_r, v_\vartheta, v_\varphi) \in \mathcal{O}_i \\ 0 & : \quad (r, \vartheta, \varphi, v_r, v_\vartheta, v_\varphi) \notin \mathcal{O}_i \end{cases} \tag{19}$$

of the image set

$$\mathcal{O}_i \equiv \bigcup_{\mathcal{W} \in \xi(\mathcal{U}_i)} \mathcal{W} \tag{20}$$

of $\mathcal{U}_i$ in phase-space. The volume of the phase-space region represented by orbit i then follows as

$$V_i = \int \chi_i \, \mathrm{d}^3 r \, \mathrm{d}^3 v \tag{21}$$

and accordingly the phase-space density along the orbit reads

$$f_i \equiv \frac{w_i}{V_i}. \tag{22}$$

3.2 Orbital weights from DFs

If we reverse the application of equation (22), and assign the orbital weights according to some given DF f,

$$w_i = f_i \, V_i, \tag{23}$$

with $f_i \equiv f(I_{1,i}, \ldots, I_{n,i})$ now being the DF f evaluated at the orbit's position in integral space, then the DF f_{lib} of the entire library, which consists of the combined contributions of all orbits

$$f_{\mathrm{lib}} = \sum_i f_i \chi_i \tag{24}$$

will be the mapped version of f on to the library. Equation (23) together with equations (6), (8) and (9) can be used to calculate the LOSVDs, internal velocity profiles and density distribution of any axisymmetric DF with known potential.

4 ORBITAL PHASE-VOLUMES

Two degrees of freedom. Binney, Gerhard & Hut (1985) have shown, that for autonomous Hamiltonian systems with two degrees of freedom the phase-volume of any orbit can be derived from the SOS by integrating the times between successive orbital visits of the SOS

$$V \approx \Delta E \int_{\mathrm{SOS}} T(r, v_r) \, \mathrm{d}r \, \mathrm{d}v_r, \tag{25}$$

where $T(r, v_r)$ is the time the orbit needs from (r, v_r) to the next intersection with the SOS, and ΔE defines a small but finite cell around the orbit's actual energy E characterizing the hypersurface in phase-space represented by the orbit.

Axisymmetric case. Richstone et al. (in preparation) carry over this result to axisymmetric systems and approximate the phase-volumes as

$$V \approx \Delta L_z \, \Delta E \int_{\mathrm{SOS}} T(r, v_r) \, \mathrm{d}r \, \mathrm{d}v_r. \tag{26}$$

Here ΔL_z and ΔE stand for the range of energies and angular momenta represented by the orbit under consideration. Equation (26) is valid independent from the orbit beeing regular or chaotic.

Calculating the SOS-integral. In what follows we describe our novel implementation of equation (26) that improves on the method of Richstone et al. (in preparation) to deliver higher precision phase-space volumes.

For all orbits in a sequence with common energy E and angular momentum L_z we obtain a representative sample $\mathcal{S}$ of the SOS by storing N_{sos} imprints of each orbit in the SOS given by the radial positions and velocities[2] at the times $t_i^{k(s)}$ of the orbital equatorial crossings,

$$\begin{aligned}\mathcal{S} \equiv \big\{&(r_i^s, v_i^s) : r_i^s \equiv r(t_i^{k(s)}), v_i^s \equiv |v_r(t_i^{k(s)})|, \\ &E_i = E, L_{z,i} = L_z, 1 \leqslant s \leqslant N_{\mathrm{sos}}\big\}.\end{aligned} \tag{27}$$

Typically, we integrate each orbit up to $N_{\mathrm{sos}} = 80$ intersections with the SOS and choose $N'_{\mathrm{sos}} = 60$ points for the calculation of the phase-volumes randomly out of the whole set of intersections. We also store the time intervals

$$t(r_i^s, v_i^s) \equiv t_i^{k(s+1)} - t_i^{k(s)} \tag{28}$$

between two successive intersections.

Inspection of Fig. 1 shows that only a tessellation approach can numerically integrate equation (26) in the general case including regular, resonant and chaotic orbits. To this purpose we decided to perform a Voronoi tessellation of $\mathcal{S}$ using the software of Shewchuk (1996). This tessellation uniquely allocates a polygon to each element of $\mathcal{S}$. The edges of the polygon are located on the perpendicular bisections of pairs containing the element under consideration and one of its neighbours and are equidistant to the actual pair and a third element. For almost all elements the polygons are closed and encompass an area containing the actual element

[2] To reduce the computational effort we take the absolute value of the radial velocities, thereby exploiting the symmetry of the SOS with respect to the r-axis in our application.

and all points that are closer to it than to any other element. The areas enclosed by the polygons completely cover the space between the elements and therefore characterize the fractional area inside the SOS occupied by each orbit.

Fig. 2 shows the same SOS as Fig. 1. The open circles display r and v_r at the orbital equatorial crossings. The thin lines around these circles mark the Voronoi cells, e.g. the polygons allocated to the elements of $\mathcal{S}$ and boundary points (see below).

With ΔA_i^s beeing the surface area enclosed by the polygon around $(r_i^s, v_i^s) \in \mathcal{S}$ the integral expression in the phase-volume of orbit i (cf. equation (26)) can be approximated[3] as

$$\int_{\mathrm{SOS}} T(r, v_r)\,\mathrm{d}r\,\mathrm{d}v_r \approx \sum_s t(r_i^s, v_i^s)\ \Delta A_i^s. \tag{29}$$

At the boundary of the distribution of sampled points, there may not be enough neighbours around a given element of $\mathcal{S}$ to close its polygon. In order to ensure that every Voronoi polygon is closed and confined to an area enclosed by the ZVC of the SOS (given by v_r of equation (11)) we construct an envelope around the distribution of sampled orbital intersections. In Fig. 2 the points of the envelope are marked by the solid dots. They are constructed as follows.

In a first step, we determine the maximum $\hat{v}_0$ of radial velocities in $\mathcal{S}$

$$\hat{v}_0 \equiv \max\left\{v_r : (r, v_r) \in \mathcal{S}\right\}. \tag{30}$$

To ensure that no Voronoi cell exceeds below the axis $v_r = 0$, all imprints in the SOS with $v_i^s \leqslant \epsilon\,\hat{v}_0$ are mirrored about the axis $v_r = 0$ (typically $\epsilon = 0.1$). For the rest of the SOS we construct an envelope in an iterative loop starting from

$$(\hat{r}_0, \hat{v}_0) \equiv (r, v_r) \in \mathcal{S},\ v_r = \hat{v}_0. \tag{31}$$

In each iteration $n+1$ we search for $(\hat{r}_{n+1}, \hat{v}_{n+1}) \in \mathcal{S}$ obeying

$$\hat{v}_{n+1} = \max\left\{v_r : (r, v_r) \in \mathcal{S},\ r > \hat{r}_n\right\}. \tag{32}$$

We compose the envelope out of points densely sampled from the line segment connecting (r'_n, v'_n) and (r'_{n+1}, v'_{n+1}), where the prime indicates that the coordinates are slightly shifted outwards, i.e. $r'_n = (1+\delta)\hat{r}_n$ and $v'_n = (1+\delta)\hat{v}_n$ with typical $\delta = 0.01$. The loop eventually stops after N iterations at $\hat{r}_N = r_{\mathrm{up}}$ and is followed by an analogous procedure running from $\hat{r}_0$ to r_{lo} to complete the envelope along the left part of the SOS. The points on the envelope are used as additional seeds for the Voronoi tessellation.

As Fig. 2 shows, the apposition of the boundary points as described above ensures that all orbital Voronoi cells are closed and confined to an area roughly bounded by the outermost invariant curve of the SOS. The definition of the boundary is purely geometrical and insensitive to numerical uncertainties in the orbit integration. The spiky cells along the upper boundary belong to seeds of the envelope and do not affect the calculation of the orbital phase-volumes.

[3] Note that the Poincaré map of the SOS on to itself is area-preserving and one would like to have ΔA_i^s independent of s. The Voronoi tessellation however yields only approximately constant ΔA_i^s. Nevertheless, as Sec. 5 shows, the resulting phase-volumes are of high accuracy.

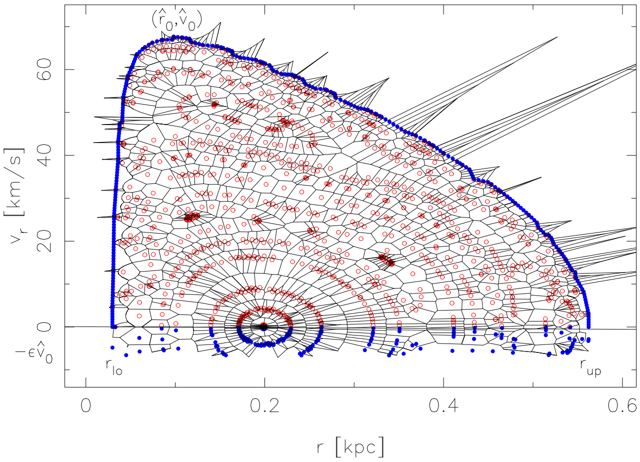

Figure 2. A Voronoi tessellation of the SOS of Fig. 1. Open circles mark individual intersections of orbits with the SOS, solid dots are points added to get the Voronoi cells well behaved at the boundaries.

The Voronoi tessellation used to approximate the integral expression in equation (26) via equation (29) defines a robust method to calculate the relative phase-volume of any orbit inside a particular sequence of orbits with common E and L_z, including resonances and chaotic orbits. The areas assigned to the individual orbital imprints in the SOS completely fill the area below the ZVC of the SOS. Thus, a cruder sampling of the SOS is compensated by larger individual orbital phase-volumes. In the limit of an infinitely dense sampling, the assigned "phase-space-weights" obtained by the tessellation approach single-orbit phase-volumes.

Calculating $\Delta E\,\Delta L_z$. For a complete determination of the phase-volumes we also need the relative contribution of a whole sequence of orbits with common (E, L_z) as compared to other sequences with different energies and angular momenta. These are described by the factors $\Delta L_z\,\Delta E$ of the orbital phase-volumes (cf. equation (26)). They are in fact equal for all orbits in the same sequence and need to be calculated only once for each sequence.

Fig. 3 shows an example of the (E, L_z)-plane of a typical library. The dots display the grid of sampled orbital energies and angular momenta. Each dot represents a sequence of orbits with common E and L_z but different I_3. To calculate $\Delta L_z\,\Delta E$ for a particular sequence, we construct a quadrangle around the sequence's (E, L_z) and estimate the product $\Delta L_z\,\Delta E$ as the surface area enclosed by this quadrangle. The thin lines in Fig. 3 show the boundaries of these quadrangles, which are constructed as follows.

As described in Sec. 2.1 the grid in (E, L_z)-space is derived from the requirement that for every pair $r_i < r_j$ of equatorial grid bins, the library contains at least one equatorial orbit with $r_{\mathrm{peri}} = r_i$ and $r_{\mathrm{apo}} = r_j$. Consider now a sequence of orbits with $(E_{\mathrm{seq}}, L_{z,\mathrm{seq}})$ and corresponding $r_{\mathrm{peri,seq}}$ and $r_{\mathrm{apo,seq}}$ of the equatorial orbit. In (E, L_z)-space all sequences inside the boundary of the sampled area are surrounded by four other sequences having both their peri- and their apocenter in adjacent spatial bins. Let $r_{\mathrm{peri},j}$ and $r_{\mathrm{apo},j}$, $1 \leqslant j \leqslant 4$, denote the corresponding peri- and apocenters of the equatorial orbits of these sequences. We con-

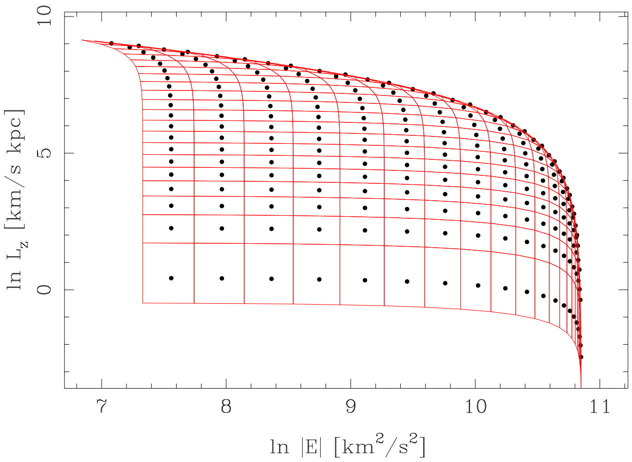

Figure 3. Typical distribution of sampled energies E and angular momenta L_z of an orbit library. The thin red lines show the boundaries of small cells assigned to each sequence. Their surface area is taken to estimate $\Delta E\,\Delta L_z$. The potential equals that of Figs. 1 and 2.

struct a quadrangle around the sequence $(E_{\rm seq}, L_{z,{\rm seq}})$ by connecting the energies and angular momenta of four fictitious orbit sequences characterised by the pericenter $\hat{r}_{{\rm peri},j}$ and apocenter $\hat{r}_{{\rm apo},j}$ of their equatorial orbits

$$\hat{r}_{{\rm peri},j} = \frac{1}{2}(r_{{\rm peri},j} + r_{\rm peri,seq}) \tag{33}$$

and

$$\hat{r}_{{\rm apo},j} = \frac{1}{2}(r_{{\rm apo},j} + r_{\rm apo,seq}). \tag{34}$$

The sequences with the largest apocenters and the smallest pericenters, respectively, are surrounded by less than four sequences having both their peri- and their apocenter in adjacent spatial bins. For these sequences we calculate the edges of the quadrangle as if there were further sequences around, whose energies and angular momenta follow from our spatial grid at smaller radii than $r_{\rm min}$ and larger radii than $r_{\rm max}$.

Sequences with $r_{\rm peri,seq} \approx r_{\rm apo,seq}$ (lying on the upper boundary of the sampled area in Fig. 3 and usually containing only one, approximately circular, orbit) are also not surrounded by four sequences as described above. For these sequences we take $(E_{\rm seq}, L_{z,{\rm seq}})$ of the actual sequence as the upper right edge of the quadrangle.

As can be seen in Fig. 3 the quadrangles around the sequences' energies and angular momenta completely cover the sampled part of the allowed area in (E, L_z)-space below the curve $L_z(E) = L_{z,{\rm circ}}$. They give a reasonable measure of the fractional area in (E, L_z)-space, occupied by each orbit sequence.

5 MAPPING DISTRIBUTION FUNCTIONS ON TO THE LIBRARY

In this Section we describe how to use the phase-volumes from the previous Section to calculate internal and projected properties of stationary DFs using an orbit library. To this end, starting with a density profile ρ and a stationary distribution function f_ρ connected to ρ via $\rho = \int f_\rho \, {\rm d}^3 v$, a library is constructed as described in Sec. 2. Instead of fitting the library to the kinematics of f_ρ,

$$\mathrm{LOSVD}_f(v_{los}) = \frac{1}{\rho}\int f_\rho \, {\rm d}^2 v_\perp \tag{35}$$

we *assign* an appropriate weight to each orbit such that the superposition of all orbits represents f_ρ (see Sec. 3.2 above). We then compare the internal density distribution $\rho_{\rm lib}$ and the anisotropy profile $\beta_{\rm lib}$, as well as the projected kinematics $\mathrm{GHP}_{\rm lib}$ obtained from the library with the same properties ρ, β and GHP directly calculated from the DF (see Sec. 5.1 - 5.2). Thereby we can check to which accuracy the orbit library reproduces a *given* dynamical system.

5.1 Spherical γ-models

As a first reference case, we explore spherical γ-models.

Properties of the input model. The stellar body of the reference model is constructed from γ-models (Dehnen 1993) with density

$$\rho_\gamma(r) = \frac{M}{4\pi}\frac{r_s(3-\gamma)}{r^\gamma (r_s + r)^{4-\gamma}}. \tag{36}$$

They approximate the de Vaucouleurs law of ellipticals quite well for $\gamma \in [1, 2]$. The DF is assumed to be of the Osipkov-Merritt type $f_{\rm OM} = f_{\rm OM}(E - L^2/2r_a^2)$ (Osipkov 1979; Merritt 1985a; Merritt 1985b). The corresponding systems are isotropic at $r \ll r_a$ and radially anisotropic at $r \gg r_a$:

$$\beta \equiv 1 - \frac{v_\vartheta^2 + v_\phi^2}{2\,v_r^2} = \frac{r^2}{r^2 + r_a^2}. \tag{37}$$

We tested various combinations of the parameters (γ, r_s, r_a). However, since the conclusions drawn from the comparisons do not depend strongly on γ, the following contains only a discussion of the results for the Hernquist model ($\gamma = 1$), where the DF can be written in terms of elementary functions and reads (Hernquist 1990)

$$f(E,L) \propto \frac{1}{8(1-q^2)^{5/2}} - 3\arcsin q + (1-2q^2) \left(q\sqrt{1-q^2}(8q^4 - 8q^2 - 3) + \frac{r_s^2}{r_a^2} q \right) \tag{38}$$

with $q = \sqrt{r_s(E - L^2/2r_a^2)/GM}$.

Comparison of model and library. Fig. 4 shows the GHPs, density and anisotropy profiles of a library with $\approx 2 \times 8800$ orbits, extending from $\approx 5 \times 10^{-4}\, r_s$ to $\approx 28\, r_s$. For this library we have used a closed meshed sampling containing two different pericenters for each radial bin. The weights for the orbits were directly derived from equation (23) and the Hernquist DF of equation (38) with $r_s = 10.5\,$kpc, a total mass of $M = 7.5 \times 10^{11} {\rm M}_\odot$ and $r_a = \infty$ (isotropic model). The big dots show the expected kinematics, density and anisotropy of the Hernquist model. The GHPs were obtained by first calculating the LOSVDs at the position of the corresponding spatial bin from the DF using the method described in Carollo, de Zeeuw & van der Marel (1995) and then fitting a GH-series to the LOSVDs. For the density distribution and anisotropy we used equations (36) and (37), respectively.

As the figure shows, the library is able to reproduce the GHP and internal density distribution of the model to a high degree of accuracy. The mean fractional difference in σ is below $\Delta\sigma < 1$ per cent and the mean difference in H_4 is below $\Delta H_4 < 0.01$. The largest deviations between model and library occur in the anisotropy profile with $\mathrm{rms}(\beta) = 0.06$ (taken over a whole angular ray). The individual differences however are smaller than $\Delta\beta = 0.1$ over almost the whole spatial range covered by the library. Near the inner and outer boundary of the library the orbit sampling becomes incomplete with mostly radial orbits coming either from outside the outer boundary or from inside the inner boundary are missing. Consequently, the library shows a decrease in radial velocity dispersion ($\beta < 0$) as compared to the expectations of the isotropic reference model.

Fig. 5 shows the same as Fig. 4 but for an anisotropic Hernquist model with $r_a = 4\,r_s$. It confirms the results from the isotropic model. The offset in the H_4-profiles at large radii is due to errors in the GH-fit. At these radii the resolution of our LOSVD-bins is too low to give reliable GHPs. However the match of the individual LOSVDs itself is as good as at smaller radii.

Again the largest deviations show up in the β-profiles, with a mean $\mathrm{rms}(\beta_{\mathrm{hern}} - \beta_{\mathrm{lib}}) = 0.03$. As in the isotropic case the differences between model and library increase when approaching the edges of the library, where the radial velocity dispersion of the library is systematically lower than expected.

5.2 Flattened Plummer model

We now go one step further and use a *flattened* test object, namely the flattened Plummer model of Lynden-Bell (1962) (normalized such that in the spherical limit M defines the total mass of the model)

$$\rho_{\mathrm{pl}}(r,\vartheta) = \frac{M\lambda^{-9/4}}{4\pi}[\left(3a^2 - 2b^2\right)\left(r^2 + a^2\right)^2 + \left(4a^2 - b^2\right) b^2 r^2 \cos^2(\vartheta)], \tag{39}$$

$\lambda = \left(r^2 + a^2\right)^2 - 2b^2 r^2 \cos^2(\vartheta)$. The parameters a and b describe the extension of the core and the flattening. The part of the distribution function, which is even in L_z is

$$f_{\mathrm{pl}}(E, L_z) = \frac{\sqrt{2}}{4\pi^{3/2}}\left(\frac{\Gamma(6)}{\Gamma(\frac{9}{2})} D E^{\frac{7}{2}} + \frac{\Gamma(10)}{\Gamma(\frac{15}{2})} C L_z^2 E^{\frac{13}{2}}\right), \tag{40}$$

$C \propto (3a^2 - 2b^2)$ and $D \propto 5b^2(2a^2 - b^2)$. The Plummer models do not rotate as long as the uneven part of f_{pl} vanishes and prograde and retrograde orbits exactly balance each other.

Comparison of model and library. Fig. 6 shows a flattened Plummer model with $a = 5.0\,\mathrm{kpc}$, $b = a/2$ and $M = 7.5 \times 10^{11}\mathrm{M}_{\odot}$ (big dots) and profiles obtained from a library with $\approx 2 \times 4400$ orbits, extending from $\approx 10^{-3}\,a$ to $\approx 20\,a$ (solid and dashed lines as in Figs. 4 and 5). The weights were derived from f_{pl} via equation (23). The kinematics along the major and the minor axis have been calculated from higher order Jeans equations (Magorrian & Binney 1994). Before determining the GH-parameters the projected moments were integrated along a 3.6 arcsec wide major-axis slit and a 2.0 arcsec wide minor-axis slit. (Note that for the axisymmetric case we take $\beta = 1 - \sigma_\vartheta^2/\sigma_r^2$.)

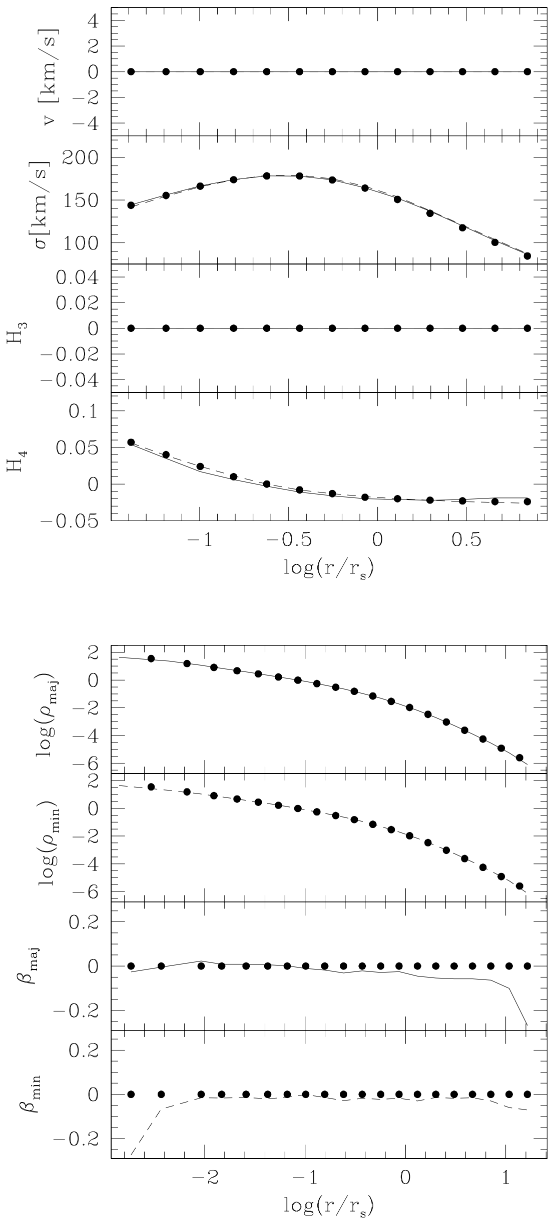

Figure 4. Comparison of a Hernquist model (big dots) and a library with weights directly derived from the spherical, isotropic Hernquist DF (lines). The upper panel shows the projected kinematics along the major axis (solid line) and minor axis (dashed line). The lower panel shows the density distribution (upper two rows, $[\rho] = \mathrm{M}_{\odot}/\mathrm{pc}^3$) and the anisotropy parameter (lower two rows) for the minor and major axis, respectively.

As in the spherical case the Gauss-Hermite parameters of the projected kinematics are reproduced to better than a few percent. Deviations in the outer parts of the H_4-profile stem from the GH-fit and are not seen in the LOSVDs. The density distribution is also well reproduced up to $\approx a/10$ and the anisotropy parameter is $|\beta| < 0.1$ from the outer edge of the library down to $\approx a/10$.

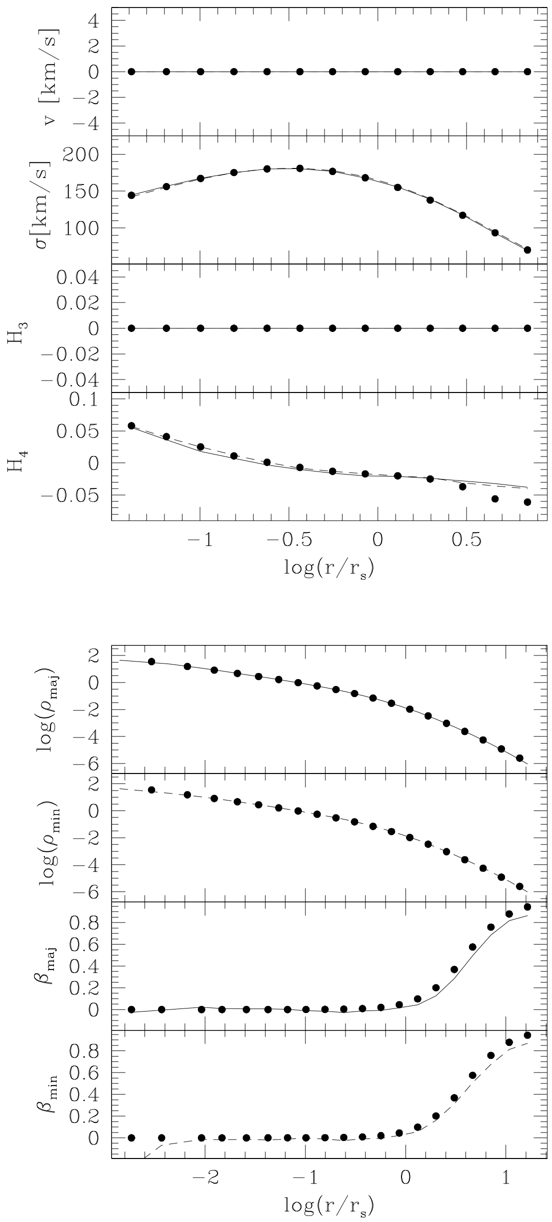

Figure 5. Same as Fig. 4 but for an anisotropic Hernquist model with $r_a = 4\, r_s$.

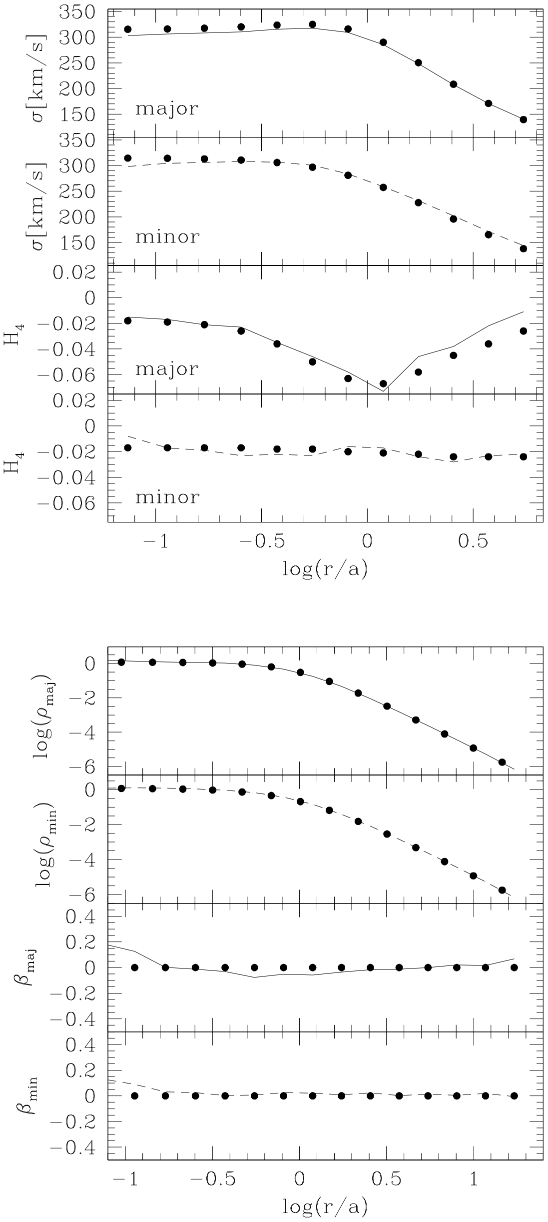

Figure 6. Comparison of a flattened Plummer model (big dots) and a library with weights directly derived from the DF (lines). Upper panel: projected kinematics along major axis (solid lines) and minor axis (dashed lines). Only moments independent from the uneven part of the DF are shown. Lower panel: density distribution (upper two rows, $[\rho] = \mathrm{M}_\odot\,\mathrm{pc}^{-3}$) and the anisotropy parameter (lower two rows) for the two axes.

5.3 Changing the spatial coverage of the library

The library only discretely represents a finite part of the available phase-space. To check how this affects the accuracy of the calculation of phasespace integrals of a given DF with the library, we did the profile comparisons described in Sects. 5.1 and 5.2 for libraries with different spatial extent and for different resolutions in the space of orbital integrals.

The upper panel of Fig. 7 shows σ and H_4 along the major and the minor axis for the isotropic Hernquist model (big dots). The four different lines show the outcome of four libraries with different spatial coverage. For the solid line ($r_{\min} = 2.5 \times 10^{-4}, r_{\max} = 10$) (in units of the effective radius), for the dotted line ($r_{\min} = 2.5 \times 10^{-3}, r_{\max} = 10$), for the short dashed line ($r_{\min} = 2.5 \times 10^{-4}, r_{\max} = 5$) and for the long dashed line ($r_{\min} = 2.5 \times 10^{-3}, r_{\max} = 5$).

As expected the less extended libraries fail to reproduce the innnermost or outermost datapoins, respectively. In the vicinity of the equatorial plane (e.g. along the major axis and at the central parts of the minor axis) the library becomes dominated by azimuthal motion, when approaching $r_{\min}$ or $r_{\max}$, since orbits coming from further outside or inside are missing. Consequently, the LOSVDs are too flat (too small

H_4) as compared to the expectations (see e.g. the outermost parts of the dashed lines of the libraries with small $r_{\max}$ along the major axis and the innermost parts of the long-dashed and pointed lines of the libraries with large $r_{\min}$ in the minor-axis H_4-profile).

The effect can also be seen in the internal dynamical structure, which is illustrated in the lower panel of Fig. 7 where the anisotropy of the library with respect to φ and ϑ is plotted separately,

$$\beta_\varphi \equiv 1 - \frac{\sigma_\varphi^2}{\sigma_r^2}, \; \beta_\vartheta \equiv 1 - \frac{\sigma_\vartheta^2}{\sigma_r^2}. \tag{41}$$

Near the centre $\beta_\varphi < 0$ along the major and minor axis, confirming the dominance of φ-motion brought about by the dominance of orbits having their inner turning points there and consequently rotate fastly around the axis of symmetry. The effect is less pronounced at the outer points of the major axis, where the effective potential of the meridional plane motion is less dominated by the L_z-term.

The β_ϑ-profiles lack from boundary effects because they are independent from the (E, L_z)-sampling and simply reflect the degree to which the SOSs are filled with orbital invariant curves.

Along the minor axis the agreement of library and model in projected σ is quite good. Near the centre the library's σ is enhanced due to the orbits having their pericenter there.

5.4 Changing the number of orbits in the library

Fig. 8 shows the same comparison as Fig. 7, but for libraries, where we have skipped every second $r_{\rm peri}$ resulting in only $\approx 2 \times 4700$ orbits per library. The gross appearance of Fig. 8 is quite similar to Fig. 7 with some minor differences. First, the scatter in the GHPs has increased a bit, however the match of predictions and library is still on a level of a few percent.

The most striking difference is the increase of radial relative to azimuthal motion near the centre of the library. Most probably this reflects the fact that the pericenters of the orbit sequences are located at the inner edge of each radial bin. Therefore the most radial orbits which contribute also significantly to v_ϕ near their turning points move through the whole bin before turning around and thus rise the radial velocity dispersion. This effect is strongest in the centre since our binning there becomes relatively large compared to the variation of the potential. The balance between radial and meridional motion is not affected by this resolution-effect, because the sampling *inside* each sequence (in the SOS) is independent from the (E, L_z)-grid and thus independent from the resolution of the sampled peri- and apocenters.

6 FITTING THE LIBRARY

So far we have omitted the problem of finding the orbital weights w_i according to some given kinematical constraints. This section contains a brief description of our use of the maximum entropy technique of Richstone & Tremaine (1988) to fit the library to some LOSVDs.

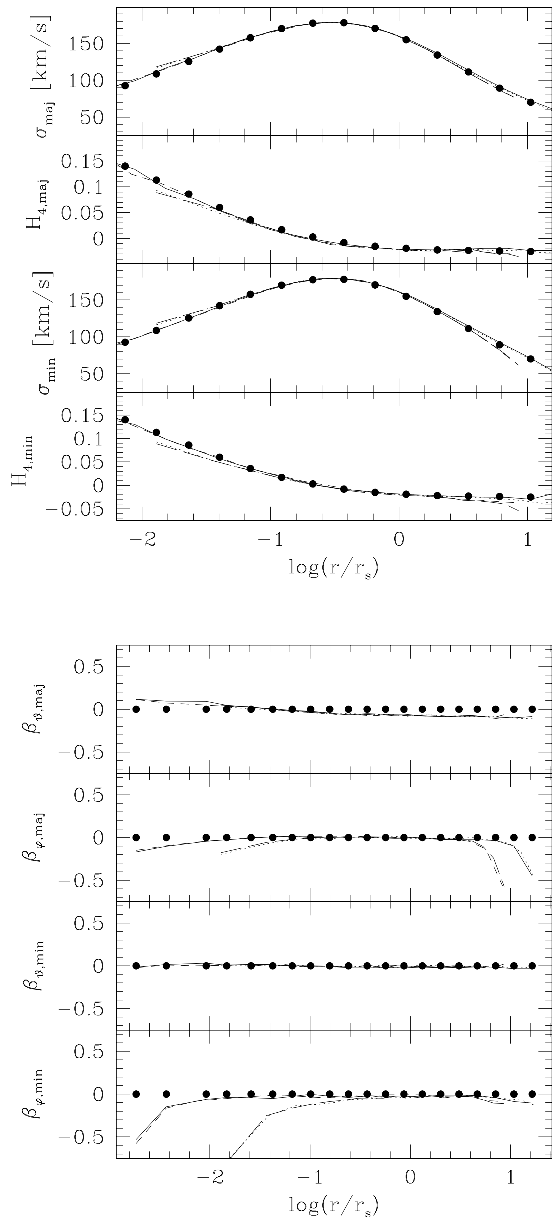

Figure 7. σ and H_4 (upper panel) and anisotropy (lower panel) along major and minor axis for the isotropic Hernquist model (big dots) and four libraries with different spatial extension $(r_{\min}/r_{\rm eff}, r_{\max}/r_{\rm eff})$: $(2.5 \times 10^{-4}, 10)$ solid line, $(2.5 \times 10^{-3}, 10)$ dotted line, $(2.5 \times 10^{-4}, 5)$ short dashed line, $(2.5 \times 10^{-3}, 5)$ long dashed line.

6.1 Maximum entropy technique

Given a set of kinematic constraints, we seek the orbital weights, that best fit the library to the constraints. These weights are derived from the maximization of an entropy-like quantity (Richstone & Tremaine 1988)

$$\hat{S} \equiv S - \alpha\chi^2, \tag{42}$$

where

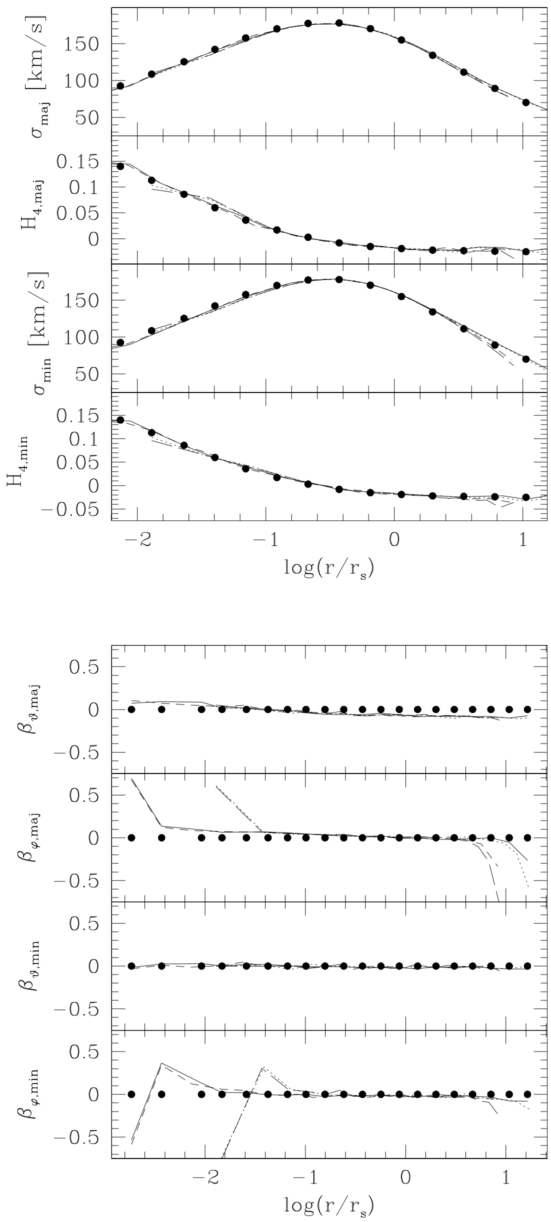

Figure 8. Same profiles as in Fig. 7, but the libraries have been set up with a coarser sampling with roughly half the number of orbits as compared to Fig. 7.

$$\chi^2 = \sum_{j,k} \left(\frac{\mathrm{LOSVD(lib)}^{jk} - \mathrm{LOSVD(data)}^{jk}}{\Delta \mathrm{LOSVD(data)}^{jk}} \right)^2 \tag{43}$$

gives the departure between the predicted kinematics of the library LOSVD(lib) (cf. equation (9)) and the data kinematics LOSVD(data) . Note that the luminosity density ν is not fitted, but used as a boundary condition (see Richstone et al. (in preparation) for details). S is an approximation to the usual Boltzmann-entropy

$$S \equiv \int f_{\rm lib} \ln \left(f_{\rm lib} \right) \, \mathrm{d}^3 r \, \mathrm{d}^3 v \; = \sum_i w_i \ln \left(\frac{w_i}{V_i} \right). \tag{44}$$

In the absence of any other condition the maximization of S enforces the weights w_i to be proportional to the phase-volumes V_i. This fact can be used to bias the library towards any set of predefined weights. If, for example, we substitute the phase-volumes in equation (44) by $V_i \rightarrow f_i \, V_i$,

$$S \rightarrow S' = \sum_i w_i \ln \left(\frac{w_i}{f_i \, V_i} \right), \tag{45}$$

then the maximization of S' yields weights w_i proportional to $f_i \, V_i$. According to equation (23) one can choose the factors f_i to bias the library towards any given DF f. The Boltzmann entropy corresponds to the case of equal a priori probabilities $f_i = f_j$ in phase-space.

6.2 The smoothing parameter α

The smoothing parameter α controls the influence of the entropy S on the fitted weights. If α is small, then the maximum of $\hat{S}$ is less affected by χ^2 and the library gives a poor fit to the data. Consequently, it will not represent the true structure of the object to which it is fitted. If on the other hand α is large, then the maximum of $\hat{S}$ is mostly determined by the minimum of χ^2. In this case the library fits the noise in the data. The DF of the library is then highly unsmooth and again does not represent the true DF of the corresponding object.

The question of how much smoothing has to be applied in order to get an optimal estimate of the true underlying DF for a given set of observational data with specific errors and spatial sampling will be the content of a forthcoming paper. Here, we focus on illustrating the accuracy of our method to setup the orbit libraries. In the following we will always show the results for that α which gives the best match to the input DF.

7 RECONSTRUCTING DISTRIBUTION FUNCTIONS FROM FITTED LIBRARIES

In this Section we use the DFs of Sec. 5, but instead of exploiting equation (23) to *assign* the orbital weights and to compare spatial profiles of the library and the original DF, we now fit the library to the DF as follows. First, we calculate the density profile and GHPs connected with the DF

$$\rho = \int f \, \mathrm{d}^3 v \tag{46}$$

and

$$\mathrm{LOSVD}_f(v_{los}) = \frac{1}{\rho} \int f \, \mathrm{d}^2 v_\perp \tag{47}$$

where the GHPs are obtained from the LOSVDs as described in Sec. 5.1. We compose a library as dscribed in Sec. 2 and fit it to the GHPs via the maximum entropy technique of Sec. 6. Finally, we compare the orbital weights $w_i(\alpha)$ resulting from the fit with those expected from the DF via equation (23). By showing that the fitted weights approximate the input DF over a large region in phase-space, we justify that we can use the degree to which the library approximates the DF as a criterium to determine the optimal amount of smoothing, which we will exploit in a subsequent paper in more detail.

In order to find the best fit weights that minimize the χ^2 of Eq.(43), we derived error bars for the LOSVDs by first assigning error bars to the GHPs and then determining LOSVD errors by means of Monte-Carlo simulations. The error for σ was choosen to linearily increase with r from 2 per cent at the innermost data point to 10 per cent for the outermost data point. For H_3 and H_4 the errors increase from 0.01 to 0.05. The definition of the errors is somewhat arbitrary since we do not add noise to the data points, but they are roughly comparable to real data error bars. Since $v = 0$ in the models, the error for v is set to $\Delta v = 2\ \mathrm{km\,s^{-1}}$. A detailed investigation of the influence of realistic errors on the accuracy of the reconstructed internal properties of a fitted library will be presented in a forthcoming paper.

7.1 Hernquist model

Fig. 9 shows a comparison of characteristic properties of a library fitted to the kinematics corresponding to the dots in the upper panel and the original DF. The definition of the lines and dots as well as the input DF are the same as for Fig. 4, the fit was obtained with $\alpha = 0.0046$. As expected the match to the kinematics and the internal density profile is excellent after the fit. The anisotropy is smaller than $|\beta| < 0.1$ over a spatial region largely exceeding the area where the LOSVDs were fitted. Only near the very centre, the minor-axis β-profile drops significantly because of the lack of radial orbits coming from inside the inner boundary of the library (cf. Sec. 5).

Fig. 10 shows the DF reconstructed from the fitted weights via equation (22) (dots) together with the input DF (thick line). Each dot represents the phase-space density along one single orbit, the densities are scaled according to $\sum w_i = \sum V_i = 1$. Over a region covering 90 per cent of the library's mass, the rms-difference between the Hernquist DF and the orbital phase-space densities is 12.1 per cent. The remaining departures between model and fit are mostly due to boundary effects arising from the discrete and finite nature of the library.

Fig. 11 shows the fractional differences of input model and library as a function of orbital energy E and angular momentum L_z. For each dot, the contributions of individual orbits with common E and L_z have been integrated. Larger dots correspond to larger differences between input DF and fitted library. From Fig. 11 one sees that the remaining deviations between library and input DF mostly stem from orbits lying at the boundary of the phase-space-region covered by the library. Since the library only contains a finite number of all orbits, the fit to the kinematics with the density as a boundary condition enforces some redistribution of orbits as compared to the original DF. For example, at the outer boundary of the library ($E \approx 0$) the fitted orbital phase-space densities are too large as compared to the input DF. These orbits compensate the cut-off in energy and contain all the light that should have been distributed along even lower bound orbits. For the same reason, the library fails to reproduce the Hernquist DF near the most bound orbits.

Fig. 12 shows the results when fitting the same library to the projected kinematics of the anisotropic Hernquist model with $r_a = 4r_s$, corresponding to the dots in the upper panel of the Figure. Again, after the fit the library perfectly reproduces the internal density profile and the projected kinematics. The mismatch in the outer parts of the H_4-profiles result from errors in the GHP-fit (cf. Sec. 5.1). However, we don't fit the library to the GHP, but directly to the LOSVD. The β-profiles of the library follow the expected curves well inside the region covered with kinematical constraints. In the outer parts however they do not follow the input model to predominant radial motion but turn back to an isotropic appearance. This is a reflection of the entropy maximization used in the fit, which forces those parts of

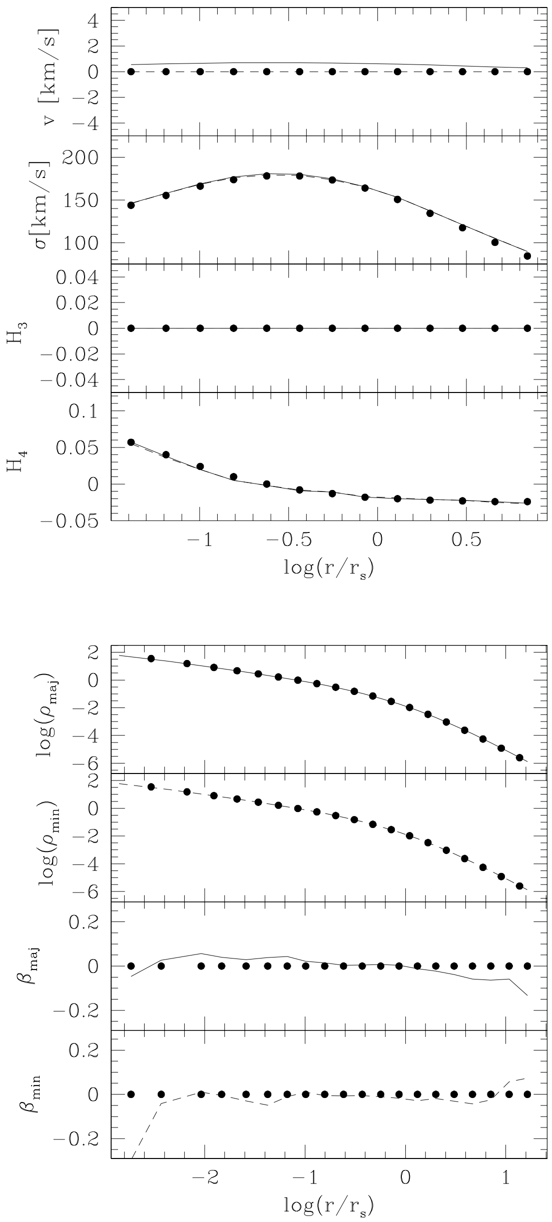

Figure 9. Comparison of a library fitted to the LOSVDs of a spherical, isotropic Hernquist DF (lines) and the Hernquist model itself (big dots). The upper panel shows the projected kinematics along the major axis (solid line) and minor axis (dashed line). The lower panel shows the density distribution (upper two rows, $[\rho] = \mathrm{M_\odot\,pc^{-3}}$) and the anisotropy parameter (lower two rows) for the two axes.

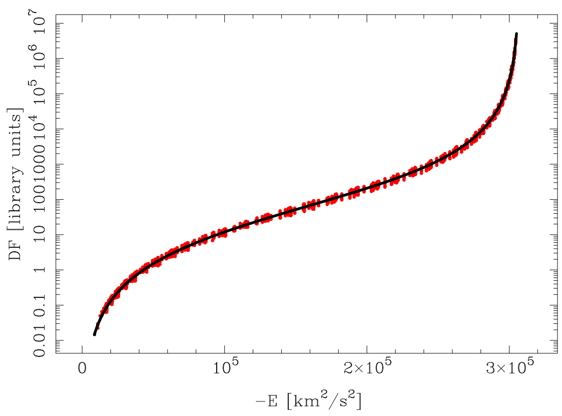

Figure 10. Comparison of the DF of a spherical Hernquist model (solid line, units defined in the text) with the phase-space densities obtained from a library fitted to GHPs along two perpendicular axes in the galaxy (details in the text). Each dot represents a single orbit. The rms between library and model is 12.1 per cent over a region covering 90 per cent of the library's mass.

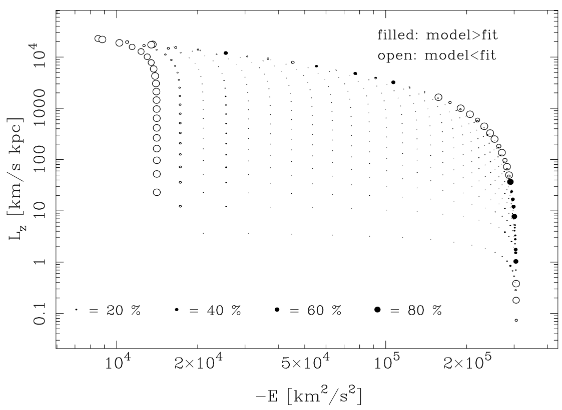

Figure 11. The fractional difference between a spherical Hernquist model and a fitted library as a function of orbital energy E and z-angular momentum L_z. Larger dots corresponds to larger differences. For open dots, the DF of the library overestimates the real DF, for the solid dots it underestimates the DF.

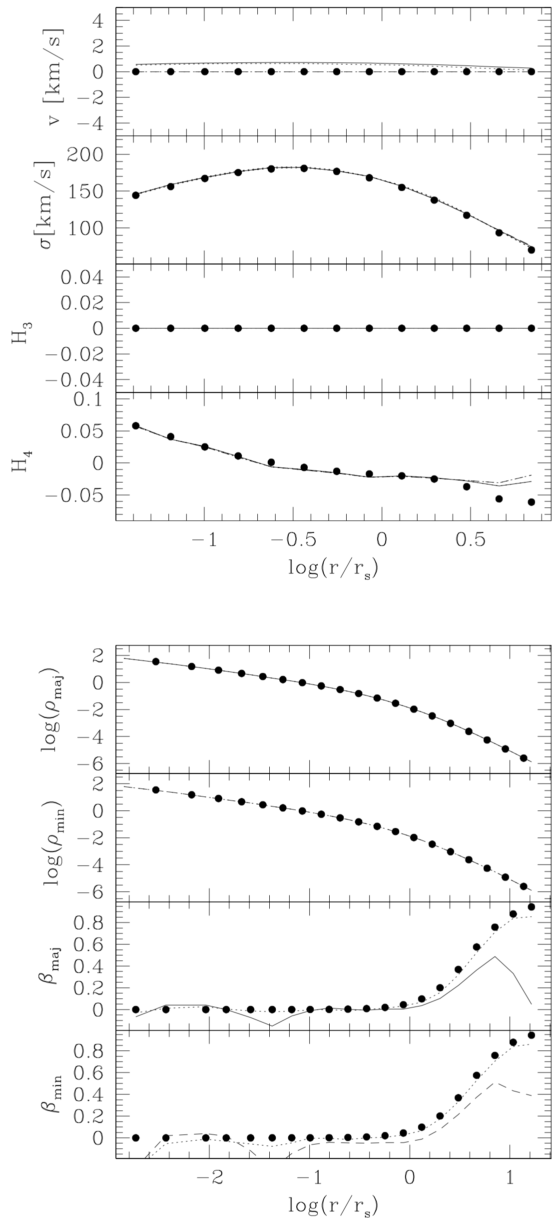

Figure 12. Same as Fig. 9 but for an anisotropic Hernquist model with $r_a = 4\,r_s$. The dotted line shows the result of a fit with "biased weights" (see text for details).

the library to isotropy, which are not constrainted by data points.

To confirm that, we refitted the library, however replaced the V_i in equation (44) by the weights of the anisotropic Hernquist DF following from equation (23). Since for the maximum entropy solution of equation (44) (without any other condition) the weights w_i are proportional to the values V_i, now being the weights of the anisotropic DF instead of the phase-volumes, this biases the fit towards the anisotropic Hernquist model. The characteristics of the corresponding fit are displayed by the dotted lines in Fig. 12. The projected kinematics and internal density are indistinguishable from the maximum entropy fit, but now the anisotropy profile is in perfect agreement with the input model.

7.2 Flattened Plummer model

Fig. 13 shows the GHPs and internal density and anisotropy of the Plummer model with $b = a/2$ of Sec. 5.2 together with a fitted library containing $\approx 2 \times 4400$ orbits. The library was fitted to the LOSVDs corresponding to the dots of the upper panel of the Figure with a smoothing parameter of $\alpha \approx 0.03$. The small deviations between the library's kinematics and the model in the upper panel of the figure are due to the low resolution in the GH-fit and are not seen in the LOSVDs used for the fit. The anisotropy parameter is confined to $|\beta| < 0.1$ all over the region where the library is constrained by kinematic data.

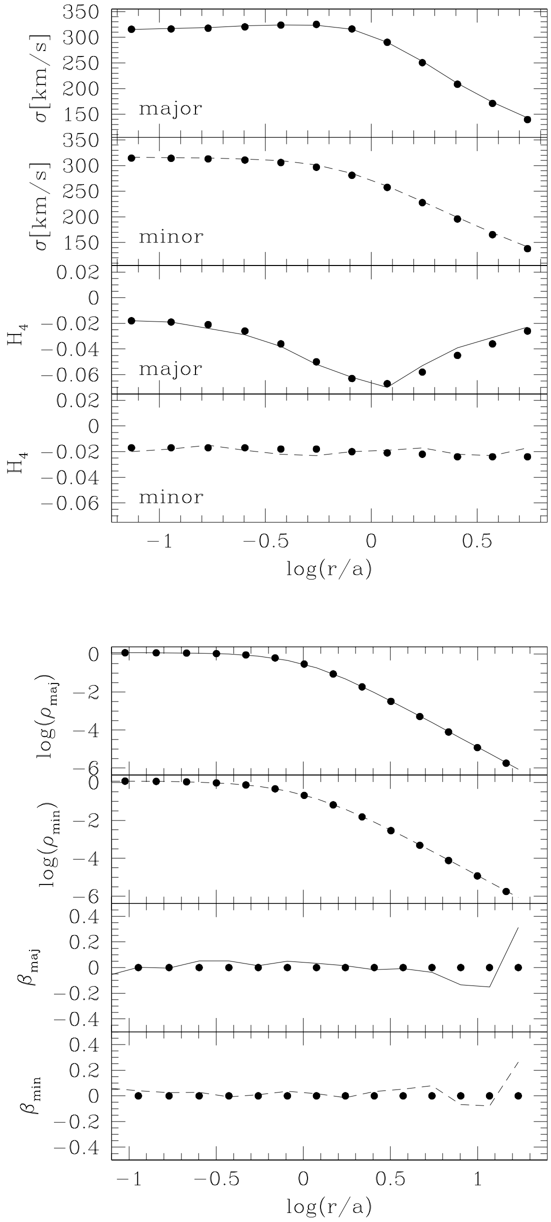

Figure 13. Comparison of a flattened Plummer model (big dots) and a fitted library (lines). The upper panel shows the projected kinematics along the major axis (solid lines) and minor axis (dashed lines). The lower panel shows internal moments along the minor and major axis, respectively (units as in Fig. 6).

The rms-difference between the reconstructed DF and the input model is ≈ 15 per cent over a region covering 90 per cent of the library's mass. As Fig. 14 shows, differences between model and library are confined to the boundaries of the sampled (E, L_z)-region of the phase-space. As for the Hernquist model, the reason for these differences is the incomplete orbit sampling at the edges of the library.

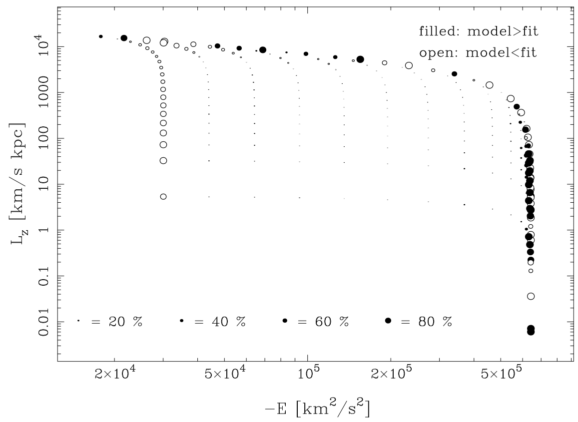

Figure 14. Deviations from the reconstructed DF of a fitted library and the Plummer DF of Fig. 13. Each dot represents one sequence of orbits with common E and L_z. For the open dots, the DF of the library overestimates the real DF, for the solid dots it underestimates it. Larger dots indicate larger differences.

8 SUMMARY

We have presented a modified version of the Schwarzschild code of Richstone et al. (in preparation). The code involves a new orbit sampling at given energy E and angular momentum L_z and a new implementation for the calculation of the orbital phase-volumes.

For our libraries we supplement the drop of orbits with common energy E and angular momentum L_z from the ZVC as described in Richstone et al. (in preparation) by scanning the SOS with a resolution that varies as the sampling progresses from the more radial to the more shell-type orbits. This sampling has been shown to completely fill the SOS connected with a pair (E, L_z) with orbital imprints.

A Voronoi tessellation of the SOSs of orbits with common E and L_z allows us to calculate the phase-space-volumes of individual orbits in any axisymmetric potential. With the phase-volumes we can convert the orbital weights describing the relative contribution of the orbits to the whole library into phase-space densities and vice versa. As a first application we use the densities to check our method to setup the library in two different ways.

First, we calculate spatial profiles of internal and projected properties of isotropic and anisotropic DFs of spherical γ-models as well as of the flattened Plummer model with the library. The density profiles, anisotropy profiles and projected kinematics of the library closely match those directly inferred from the corresponding DF. The errors in the higher order GH-parameters H_n are $\Delta H_n < 0.01$, for $n = 3, 4$ and the fractional error in the projected dispersion $\Delta\sigma < 1$ per cent are accurate on a level better than that of present day observational errors. The largest deviations occur in the anisotropy profile, but are smaller than $\Delta\beta < 0.1$ at almost all positions in the library, however increase towards the edges of the spatial region which is covered by the orbits. This boundary effect is caused by the locally incomplete orbit sampling there. If in practical applications the libraries are constructed to extend beyond the area with observational constraints, then these inaccuracies are negligible. Hence, our libraries fairly represent the phase-space structure of the considered models.

As a second application we *fitted* libraries to the GHPs of the same spherical γ-models and flattened Plummer models. The reconstructed DFs match the input DF with a rms of about 15 per cent over a region covering 90 per cent of the library's mass. The remaining deviations are mostly restricted to orbits at the boundary of the phase-space volume represented by the library. This is not unexpected since the library only discretely represents a finite subregion of the input system. Consequently some redistribution of orbits is necessary to compensate for orbits not included in the library.

We will investigate the influence of observational errors on the reconstructed DFs and of the amount of smoothing applied in the fit in a forthcoming publication. In a further step we will reconstruct the internal structure and mass composition of a sample of flattened early-type galaxies in the axisymmetric approximation.

ACKNOWLEDGMENTS

J. Thomas acknowledges financial support by the Sonderforschungsbereich 375 "Astro-Teilchenphysik" of the Deutsche Forschungsgemeinschaft.

REFERENCES

Binney J., Mamon G. A., 1982, MNRAS, 200, 361
Binney J., Gerhard O. E., Hut P., 1985, MNRAS, 215, 59
Binney J., Tremaine S., 1987, Galactic Dynamics (princeton: Princeton University Press)
Cappellari M., Verolme E. K., van der Marel R. P., Verdoes Kleijn G. A., Illingworth G. D., Franx M., Carollo C. M., de Zeeuw P. T., 2002, ApJ, 578, 787
Carollo C. M., de Zeeuw P. T., van der Marel R. P., 1995, MNRAS, 276, 1131
Cretton N., de Zeeuw P. T., van der Marel R. P., Rix H. W., 1999, ApJS, 124, 383
Cretton N., Emsellem E., 2004, MNRAS 347, L31
Dehnen W., Gerhard O. E., 1993, MNRAS, 261, 311
Dehnen W., 1993, MNRAS, 265, 250
Dejonghe H., Merritt D. R., 1992, MNRAS, 391, 531
Gebhardt K. et al., 2003, ApJ, 583, 92
Gerhard O. E., 1993, MNRAS, 265, 213
Hernquist L., 1990, ApJ, 356, 359
Lynden-Bell D., 1962, MNRAS, 123, 447
Magorrian J., Binney J., 1994, MNRAS, 271, 949
Mehlert D., Saglia R. P., Bender R., Wegner G., 2000, A&AS, 141, 449
Merritt D. R., 1985a, AJ, 90, 1023
Merritt D. R., 1985b, MNRAS, 214, 25
Merritt D. R., Saha P., 1993, ApJ, 409, 75
Osipkov L. P., 1979, Pis'ma Astron. Zh., 55, 77
Richstone D. O., Tremaine S., 1988, ApJ, 327, 82
Richstone D. O. et al, 2004, preprint, astro-ph/0403257
Rix H. W., de Zeeuw P. T., Cretton N., van der Marel R. P., Carollo C. M., 1997, ApJ, 488, 702
Romanowsky A. J., Kochanek C. S., 2001, ApJ, 553, 722
Schwarzschild M., 1979, ApJ, 232, 236
Shewchuk J., 1996, in First Workshop on Applied Computational Geometry, ACM (http://www.cs.cmu.edu/~quake/triangle.html) 124
Valluri M., Merritt D., Emsellem E., 2004, ApJ, 602, 66
van de Ven G., Verolme E. K., Cappellari M., de Zeeuw P. T., 2003, in Dark Matter in Galaxies, IAU Symposium No. 220, eds. S. Ryder, D.J. Pisano, M. Walker and K. Freeman
van der Marel R. P., Cretton N., de Zeeuw P. T., Rix H. W., 1998, ApJ, 493, 613
van der Marel R. P., Franx M., 1993, ApJ, 407, 525
Vandervoort P. O., 1984, ApJ, 287, 475
Verolme E. K., de Zeeuw P. T., 2002, MNRAS, 331, 959
Verolme E. K. et al., 2002, MNRAS, 335, 517
Wegner G., Corsini E. M., Saglia R. P., Bender R., Merkl D., Thomas D., Thomas J., Mehlert D., 2002, A&A, 395, 753

This paper has been typeset from a TEX/ LATEX file prepared by the author.